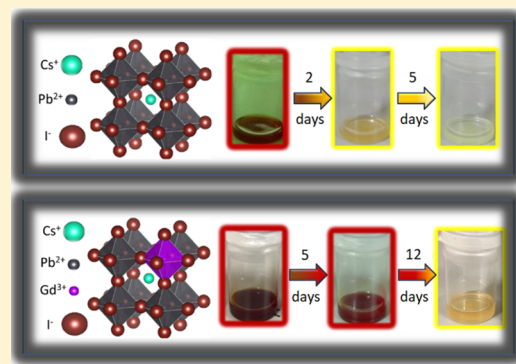


Gd³⁺-Doped α -CsPbI₃ Nanocrystals with Better Phase Stability and Optical Properties

C. Meric Guvenc,^{†,§} Yenal Yalcinkaya,^{†,§} Sercan Ozen,[‡] Hasan Sahin,^{*,‡} and Mustafa M. Demir^{*,†}

[†]Department of Materials Science and Engineering and [‡]Department of Photonics, İzmir Institute of Technology, Urla 35430, İzmir, Turkey

ABSTRACT: Black α -CsPbI₃ perovskites are unable to maintain their phase stability under room conditions; hence, the α -CsPbI₃ phase transforms into a thermodynamically stable yellow δ -CsPbI₃ phase within a few days, which has a nonperovskite structure and high band gap for optoelectronic applications. This phase transformation should be prevented or at least retarded to make use of superior properties of α -CsPbI₃ in optoelectronic applications. In this study, Gd³⁺ doping was employed with the aim of increasing the stability of α -CsPbI₃. All doped α -CsPbI₃ nanocrystals with various levels of Gd³⁺, between 5 and 15 mol %, have shown greater phase stability than that of the pure α -CsPbI₃ phase from 5 days up to 11 days under ambient conditions. This prolonged phase stability can be attributed to three potential reasons: increased tolerance factor of the perovskite structure, distorted cubic symmetry, and decreased defect density in nanocrystals. Urbach energy values suggest the reduction of defect density in the doped nanocrystals. Also, use of 10 mol % Gd³⁺ as a dopant material increases the photoluminescence quantum yield from 70 to 80% and fluorescence lifetime of α -CsPbI₃ from 47.4 to 64.4 ns. Further, density functional theory calculations are in a good agreement with the experimental results.



1. INTRODUCTION

Halide perovskites have drawn significant attention due to their high photoluminescence quantum yield, narrow emission peak, tunability, high charge carrier density, and high defect tolerance, which enable their use in applications such as light-emitting diodes, photodetectors, and solar cells.^{1–5} Furthermore, halide perovskites gain advantage against their alternatives due to their ease of producibility and remarkable potential for mass production. Despite their unique features, halide perovskites suffer from instability upon exposure to high temperature, moisture, and polar solvents.⁵ However, all-inorganic halide perovskites show better stability toward moisture, temperature, light, and heat compared to organic–inorganic halide perovskites.^{1,6}

All-inorganic perovskites have stability issues under room conditions.^{6,7} To resolve this stability handicap, various strategies have been applied to all-inorganic halide perovskites. These strategies can be classified into two groups, which are ligand modifications and doping the CsPbX₃ lattice with a different metal ion.^{8–11} In the case of ligand modifications, mainly short-chain organic cations are used for surface passivation. These ligands can reduce surface traps by introducing more halogen atoms into halogen vacancies or can passivate surface Pb atoms by binding them. For these reasons, ligand-modification-induced surface passivation causes more stable perovskite nanocrystals.^{10,11} On the other hand, doping is a method that has been used in various material systems for various applications. Doping of semiconductor nanocrystals can change the magnetic, optical, and electronic

properties remarkably since it inserts various types of atoms, which do not belong to the host crystal structure.^{12–15}

The doping strategy is widely used for increasing phase stability and optical properties of CsPbX₃ nanocrystals. Doping elements can be classified into two subgroups: isovalent and heterovalent doping elements.^{8,12} For CsPbX₃ nanocrystals, mostly used isovalent doping elements are Mn²⁺, Sn²⁺, Zn²⁺, Sr²⁺, and Ge²⁺^{16–22} as a B site dopant. Furthermore, some doping elements have been employed for A site doping such as Li, Na, K, and Rb.^{23–28} On the other hand, Eu³⁺, Al³⁺, Ce³⁺, Er³⁺, Bi³⁺, Sb³⁺, Yb³⁺, Ho³⁺, Cr³⁺, Tb³⁺, and Sm³⁺^{9,13,14,29–37} are used as heterovalent doping elements at the B site of a perovskite lattice. Akkerman et al.¹⁶ claimed that 10 mol % Mn²⁺ doping increases the stability of α -CsPbI₃ due to the smaller ionic radius of the Mn²⁺ ion, and their computational work shows that Mn²⁺ doping causes shrinking of the lattice due to shortening of the metal–halide bonds. On the other hand, Hu et al.³² used Bi³⁺ as a heterovalent dopant in CsPbI₃. The authors showed that 4 mol % Bi³⁺-doped α -CsPbI₃ has prolonged phase stability. Furthermore, they have speculated that Bi³⁺-doping-induced lattice microstrains distort the metastable cubic perovskite structure, which provides higher α -CsPbI₃ stability. Also, Jena et al.³⁴ reported that Eu³⁺ doping provides phase stability in α -CsPbI₃ thin films. Moreover, they

Received: June 22, 2019

Revised: September 16, 2019

Published: September 17, 2019



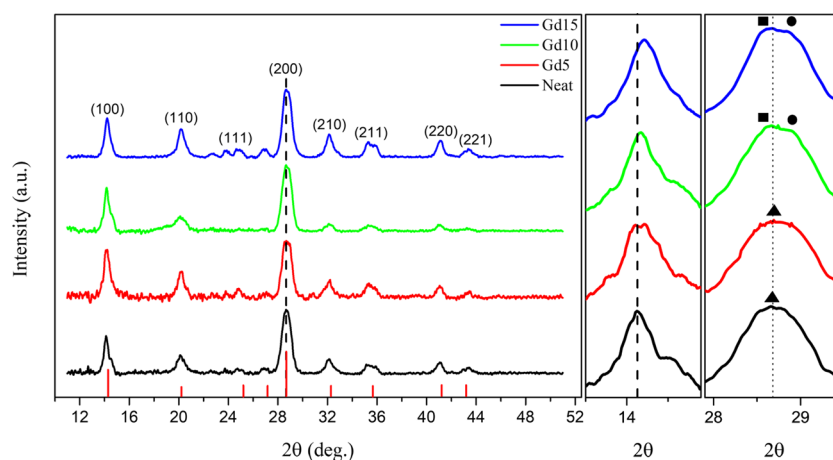


Figure 1. XRD patterns for pure, Gd5, Gd10, Gd15 nanocrystals with different Gd^{3+} concentrations. Observed peak shiftings at the (100) and (200) planes are shown. Also, peak splitting in the (200) plane is demonstrated.

relate prolonged stability of $\alpha\text{-CsPbI}_3$ with cubic lattice distortion and reduced grain size.

In this study, we investigate the influence of gadolinium doping on the structural and optical properties of CsPbI_3 nanocrystals. We observed that doping provides prolonged stability of the α -phase. Experimental results suggest that the improved phase stability is caused by the distortion of cubic symmetry, reduced defect density, and increased Goldschmidt's tolerance factor. Also, density functional theory (DFT) calculations are consistent with experimental results. Moreover, reduction of defects via Gd^{3+} doping gave rise to higher photoluminescence quantum yield (PLQY) and PL lifetime due to the increased amount of radiative recombination.

2. METHODS

2.1. Chemicals. Lead(II) iodide (PbI_2 , 99%), gadolinium acetate ($\text{Gd}(\text{CH}_3\text{CO}_2)_3 \cdot x\text{H}_2\text{O}$, 99.9% trace metal basis), cesium carbonate (Cs_2CO_3 , 99.9%, Sigma-Aldrich), 1-octadecene (ODE, 90%, Sigma-Aldrich), oleylamine (OLAM, 70%), and oleic acid (OA, 90%) were purchased from Sigma-Aldrich. Toluene ($\geq 99\%$, Merck) was purchased and used without any further purification.

2.2. Synthesis of Cs-Oleate. In a standard synthesis of Cs-oleate, 81.4 mg of Cs_2CO_3 , 4 mL of ODE, and 1.25 mL of OA were loaded in a glass tube and dried under vacuum for 1 h at 120 °C. After degassing, the temperature was increased to 150 °C under nitrogen flow, and Cs-oleate was obtained after 2 h. Before its use in the synthesis of CsPbI_3 , the Cs-oleate solution was heated to 100 °C to dissolve Cs-oleate in ODE.

2.3. CsPbI_3 and $\text{CsPb}_x\text{Gd}_{1-x}\text{I}_3$ NC Synthesis. CsPbI_3 and $\text{CsPb}_x\text{Gd}_{1-x}\text{I}_3$ nanocrystals were synthesized by the hot injection method described by Protesescu et al.¹ (with different x values for doped samples). In a typical synthesis of pure CsPbI_3 , 17.2 mg of PbI_2 (for the doped samples, $\text{PbI}_2/\text{Gd}(\text{Ac})_3$ quantities were 20.6/0.8, 19.5/1.6, and 18.4/2.4 mg), 1.25 mL of ODE, 125 μL of OA, and 125 μL of OLAM were loaded in a glass tube and dried under vacuum for 1 h at 120 °C. After degassing, the temperature was increased to 150 °C under nitrogen flow and 100 μL of Cs-oleate that is preheated to 100 °C was swiftly injected. Immediately after the injection, CsPbI_3 NCs were obtained, and 10 s after the injection, the nanocrystal solution was quenched by immersing in an ice bath and centrifuged for 15 min at 6000 rpm. The nanocrystals were

redispersed in toluene and under ambient conditions after centrifuging. Whole characterization of the samples was carried out immediately after the synthesis. After the characterization, samples were taken in glass vials for periodic XRD measurements to compare their phase stabilities.

2.4. Characterization. Scanning transmission electron microscopy (STEM) analysis of pure and doped samples was carried out to observe nanocrystals (SEM; Quanta 250, FEI, Hillsboro, OR). The samples were prepared by drop-casting diluted nanocrystal suspensions onto 200-mesh carbon-coated copper. X-ray diffraction (XRD) patterns were obtained on X'Pert Pro, Philips, Eindhoven, the Netherlands, to observe the doping effects on the lattice parameters and phase changes. All XRD samples were prepared by drop-casting a concentrated solution on a zero-diffraction quartz wafer. Absorption (Abs), photoluminescence (PL), photoluminescence quantum yield (PLQY), and time-resolved lifetime measurements were carried out on a FSS spectrofluorometer (Edinburgh Instruments, U.K.). Samples were diluted in toluene and measured in a cylindrical quartz cuvette. For Abs, a Xenon lamp was employed to scan the transmission in the 300–800 nm range. Afterward, the transmission data was transformed into Abs data. For PL and PLQY, a Xenon lamp was employed with an excitation value of 460 nm. PLQY of each sample was determined by utilizing an integrating sphere. PLQY values were obtained as average of three measurements. For LTs, the samples were excited with a 560 nm laser with a pulse width of 200 ps and a repetition rate of 1 MHz. Time-resolved lifetime measurements were recorded at 683, 686, 688, and 683 nm for neat, Gd5, Gd10, and Gd15, respectively.

2.5. Computational Methodology. Density functional theory (DFT)-based first-principles calculations were performed using projector augmented wave^{38,39} potentials as implemented in the Vienna ab initio simulation package.^{40,41} Generalized gradient approximation that is described by the Perdew–Burke–Ernzerhof functionals is used for exchange–correlation energies.⁴² The ground state calculations of a 40-atom supercell were performed until the pressure on the supercells in all directions is less than 1 kBar. For all calculations, the plane wave basis set is limited by 250 eV cut off energy and the convergence criterion for the total energy difference between sequential iterations was set to 10^{-5} eV. The Bader technique was used to analyze the partial charge transfer on the atoms.⁴³ Γ -centered k -point meshes of $3 \times 3 \times$

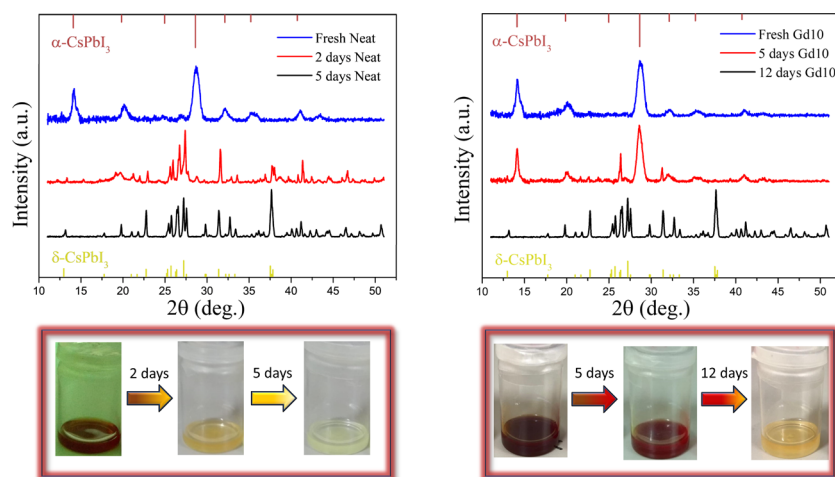


Figure 2. Time-dependent XRD patterns of neat (left) and Gd10 (right) samples and their time-dependent photographs under day light.

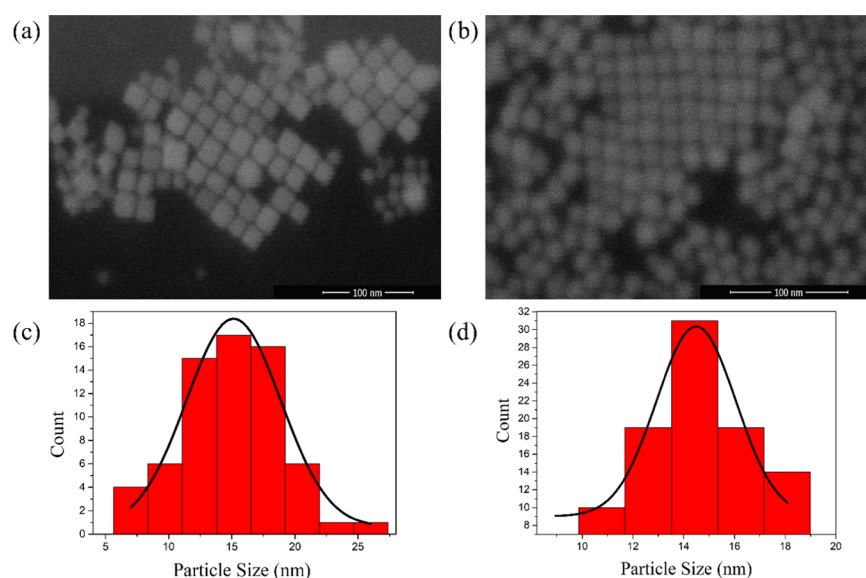


Figure 3. STEM images of different perovskite nanocrystals. Neat (a) and Gd10 (b) samples. The particle size distributions of neat (c) and Gd10 (d) samples.

3 were used. Gaussian smearing of 0.1 eV was used for electronic density of state calculations. In addition, the cohesive energies per atom for neat and Gd-doped structures were calculated using the formula

$$E_{\text{Coh}} = \left[\sum_i n_{\text{atom}(i)} E_{\text{atom}(i)} - E_{\text{system}} \right] / n_{\text{total}} \quad (1)$$

where $E_{\text{atom}(i)}$ stands for single atom energy of the i th atom (i is the number of all atoms for the same species), n_{total} is the total number of atoms in the system, and $n_{\text{atom}(i)}$ shows the number of same kind of atoms in the unit cell.

3. RESULTS AND DISCUSSION

XRD patterns of synthesized Gd³⁺-doped and neat CsPbI₃ nanocrystals are presented in Figure 1 (hereafter, 5, 10, and 15 mol % Gd³⁺-doped CsPbI₃ samples will be denoted neat, Gd5, Gd10, and Gd15, respectively). All samples have a pure cubic perovskite structure without any secondary phases. After the doping process, shifting of XRD reflections to higher angles is observed. This shifting may suggest that the doping process

successfully takes place in the perovskite structure. Peak shifting to higher angles is caused by a smaller ionic radius of the Gd³⁺ ion ($r_{\text{Gd}^{3+}} = 0.93 \text{ \AA}$) in 6-fold coordination than that of the Pb ion ($r_{\text{Pb}^{2+}} = 1.19 \text{ \AA}$). Moreover, another important observation in the XRD pattern is peak splitting of the (200) plane in the Gd10 and Gd15 samples. The splitting can be caused by reduced symmetry in the cubic perovskite structure. These lattice distortions may cause prolonged stability of the α -phase. Jena et al.³⁴ reported this peak splitting in the (200) plane in Eu³⁺-doped CsPbI₃ perovskites. The authors observed the increase in phase stability probably due to distortion of the cubic phase in the Eu³⁺-doped α -CsPbI₃ thin films. Furthermore, time-dependent XRD measurements for pure and Gd10 samples are shown in Figure 2. For neat perovskite, a high amount of α -phase transformed to the δ -phase in 2 days and it was entirely transformed into the δ -phase in 5 days. On the other hand, for the Gd10 sample, phase stability was preserved in first 4 days. δ -phase peaks began to appear first time after the fifth day in the XRD pattern. Within 12 days after synthesis, the α -phase was found to completely transform into the δ -phase and lost its cubic structure.

The ionic radius of Gd^{3+} is 0.20 Å smaller than that of Pb^{2+} in 6-fold coordination; therefore, Gd^{3+} incorporation into the perovskite lattice increases Goldschmidt's tolerance factor (eq 2)

$$t = \frac{R_X + R_A}{\sqrt{2}(R_B + R_X)} \quad (2)$$

where R_A is the radius of the A site cation, R_B is the radius of the B site cation, and R_X is the radius of the anion in the perovskite structure.^{44–46} The effective tolerance factor was calculated by the following formulas (eq 3). In these formulas, R'_B is the effective B site cation radius and t' is the effective tolerance factor

$$R'_B = (1 - x)R_{\text{Pb}^{2+}} + xR_{\text{Gd}^{3+}}, \quad t' = \frac{R_X + R_A}{\sqrt{2}(R'_B + R_X)} \quad (3)$$

When the doping ratio increased from 0 to 0.05, 0.10, and 0.15, the effective tolerance factors increased from 0.807 to 0.810, 0.813, and 0.817, respectively. The increase of the factor may result in a more stable perovskite structure.

STEM images of neat and Gd10 samples are shown in Figure 3a,b, respectively. The neat sample has a particle size of 15 ± 4 nm. On the other hand, the Gd10 sample has 15 ± 2 nm. Although the length of the particles remains unchanged after the doping process, the size distribution gets narrower with doping (Figure 3c,d). Furthermore, the PL full width at half-maximum (FWHM) decreases until 10 mol % Gd^{3+} doping, and after this level of doping, FWHM increases. This result is consistent with particle size distribution data obtained from STEM images. However, doping provides more uniform sized crystals and narrow emission peaks up to the critical doping amount (10 mol % Gd^{3+}). In Al^{3+} -doped CsPbBr_3 nanocrystals reported by Liu et al.,²⁹ the ratio of length to width (L/W ratio) was observed to be increasing from 1.11 to 1.23, which means that doping causes elongation of the nanocrystals. Also, an excitonic signal in the absorption spectrum of the doped sample is observed, which may indicate the presence of nanowires⁴⁷ or nanoplatelets,⁴⁸ while undoped CsPbBr_3 nanocubes exhibit an absorption edge. Because of discrete PL signals expected from nanoplatelets due to their strong quantum confinement and overlapping, there should be a strong blue shift in the PL spectrum in the case of morphology transformation toward nanoplatelets. Note that a similar morphology was not observed in our study when the 15% Gd^{3+} -doped sample was examined.

To observe the effect of Gd^{3+} doping in the structure, photoluminescence and absorption measurements were carried out. All samples with different Gd^{3+} amounts possess around 1.8 eV band gap. Neat perovskite shows a PL peak at 683 nm, and the PL peak slightly red-shifted from 683 to 686 nm for the Gd5 sample and 688 nm for the Gd10 sample, presented in Figure 4. Moreover, as the amount of doping increased, the PL peak blue-shifted and the Gd15 PL emission peak was observed at 683 nm. The red shift of Gd5 and Gd10 samples may be due to the formation of new states just below the conduction band upon doping.⁴⁹ However, as the dopant amounts increased, a blue shift was observed for the Gd15 sample. This blue shift may be caused by the Moss–Burstein effect.^{50,51} The Moss–Burstein effect takes place when excess n-type doping is applied on the main semiconductor structure, and this causes the occurrence of impurity sub-bands, which are partially filled within the conduction band. Formation of

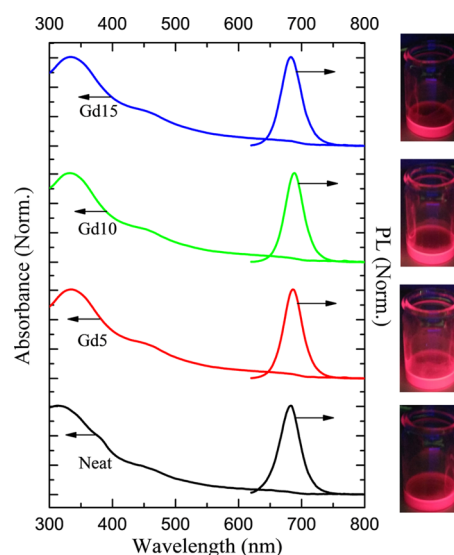


Figure 4. Absorption and PL spectra of neat and doped CsPbI_3 nanocrystals (left). Gd5 and Gd10 samples slightly red-shifted, and the Gd15 sample slightly blue-shifted. Photographs of samples under 245 nm UV light (right).

these sub-bands is caused by the interaction between the dopant states. The possibility of this interaction increases as the level of doping increases. When the Fermi level lies within the conduction band, i.e., extra electrons are introduced to the structure, higher levels of impurity sub-bands get occupied. Therefore, this behavior causes emission from the higher states and a blue shift in the PL spectrum is observed. Moreover, the PL peak of Gd10 is the narrowest among all samples, while Gd15 has a wider PL peak compared to Gd10. PL FWHM values for neat, Gd5, Gd10, and Gd15 samples are 39.0, 34.5, 34.0, and 37.0 nm, respectively. Previously, the PL signal at 683 nm and the FWHM value of 39 nm were observed for neat CsPbI_3 , which shows that our results are consistent with the literature.¹

Urbach tails of all samples were examined for comparison of defect densities of the perovskite structures. In semiconductors and insulators, the essential absorption edge below the energy band gap increases exponentially, and the absorption edge is known as the Urbach tail.⁵² For further understanding of this mechanism, absorption coefficient versus photon energy graphs are plotted for all samples. The logarithmic part of the absorption coefficient is fitted using Urbach's rule (eq 4)

$$\alpha(E) = \alpha_0 \exp \left[\sigma(T) \frac{E - E_0}{k_B T} \right] \quad (4)$$

where $\alpha(E)$ is the absorption coefficient as a function of the photon energy; E , E_0 , and α_0 are the characteristic parameters of the material; $\sigma(T)$ is the steepness factor; k_B is the Boltzmann constant; and T is the absolute temperature.

The slope of these fits was used for the calculation of Urbach energy. Urbach energy gives information about the electronic or structural disorder in the material. Urbach tails and calculated Urbach energies are represented in Figure 5a,b for all samples, respectively. The Urbach energy decreases from 14.1 meV (for neat $\alpha\text{-CsPbI}_3$) to 12.19 and 11.4 meV for Gd5 and Gd10 samples, respectively. After that, it increases to 11.7 meV for the Gd15 sample. This data implies that Gd^{3+} doping decreases the defect density in the structure up to a critical

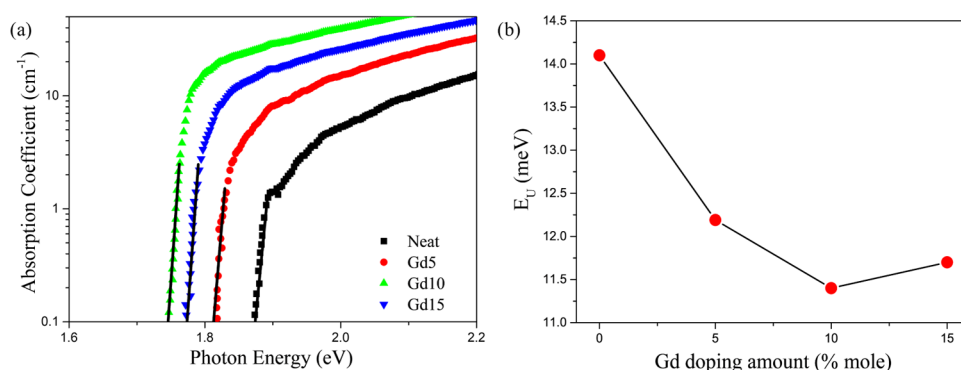


Figure 5. Absorption coefficients of all samples on a logarithmic scale (a) and their Urbach energies (b).

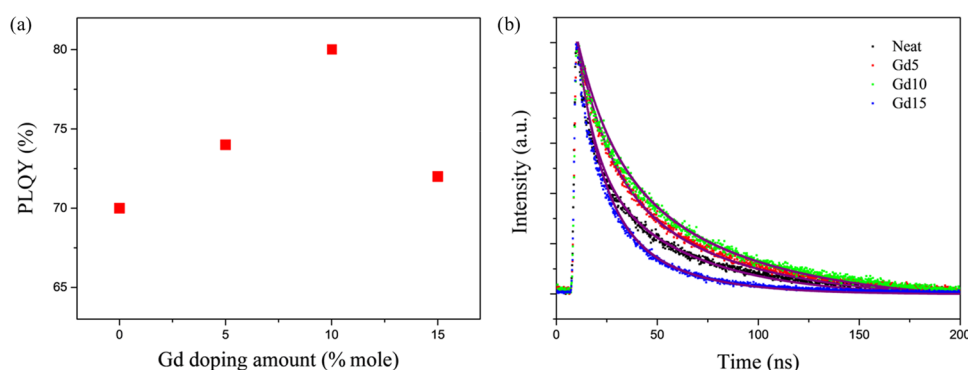


Figure 6. PLQYs of all samples excited with 460 nm wavelength light (a). Time-resolved fluorescence lifetimes of all samples excited by a 560 nm laser and collected lifetime decays fitted with the biexponential function (b).

doping concentration, after which, doping promotes trapping defects in the structure; thus, the Urbach energy for the Gd15 sample slightly increases. Similar behavior was also observed in Sb^{3+} -doped CsPbBr_3 nanocrystals by Zhang et al.,³⁶ and they reported that the Urbach tail gradually decreased up to a certain point and at higher doping amounts, it increased again. This shows that heterovalent Sb^{3+} doping decreases the defect amount in the nanocrystals up to a critical doping concentration, and after exceeding that critical concentration, the defect amount increases. As another example, Liu et al.¹⁹ reported that the Urbach energy increases with the Sn^{2+} alloying ratio in $\text{CsPb}_x\text{Sn}_{1-x}\text{I}_3$ nanocrystals and the phase stability of α - CsPbI_3 decreases. In this particular case, Urbach energies of all doped samples are higher than those of the pure phase. This is also consistent with the experimental observations since the α -phase of all doped samples is more stable than the α -phase of the neat sample and contains fewer defects than the neat sample.

As can be seen in Figure 6a, the photoluminescence quantum yield (PLQY) values of the neat, Gd5, Gd10, and Gd15 samples are 70, 74, 80, and 72%, respectively. Undoubtedly, Gd^{3+} doping into the CsPbI_3 structure causes an increase in the PLQY. This increase may arise from the defect reduction effect of the Gd^{3+} ion that enhanced radiative recombination. Liu et al.²⁹ suggest that Al^{3+} doping results in extra halide incorporation in the lattice. This increase may be caused by the reduction of defects due to extra I^- incorporation as a result of the heterovalent doping. Further, decrease in the Urbach energy is also consistent with reduced defect amount in the nanocrystals. On the other hand, time-resolved fluorescence lifetime measurements were carried out on the prepared samples and are shown in Figure 6b.

Fluorescence lifetime curves were fitted with the biexponential function to calculate slow (radiative recombination) and fast (nonradiative recombination) components. Obtained data from fitted fluorescence lifetime curves is shown in Table 1.

Table 1. Time-Resolved Photoluminescence Lifetime Profiles for CsPbI_3 Nanocrystal Different Doping Ratios, Which Are Fitted with a Biexponential Function

sample	τ_1	τ_2	A_1	A_2	τ_{avg}
neat	9.2	48.8	15.6	84.4	47.4
Gd5	15.6	60.2	19.8	80.2	57.5
Gd10	16.3	66.3	14	86	64.4
Gd15	11.4	34.3	33.6	66.4	31

Radiative components of neat, Gd5, Gd10, and Gd15 nanocrystals are 48.8, 60.2, 66.3, and 34.3 ns, respectively. Their contributions to the average lifetimes (τ_{avg}) are 84.4, 80.2, 86, and 66.4%, respectively. The average lifetime was calculated using the following equation (eq 5), where A_1 and A_2 are the constants and τ_1 and τ_2 are the slow and fast recombination times, respectively

$$\tau_{\text{avg}} = \frac{A_1\tau_1^2 + A_2\tau_2^2}{A_1\tau_1 + A_2\tau_2} \quad (5)$$

Moreover, the calculated average lifetime increases from 47.4 ns for neat perovskite to 64.4 ns for the Gd10 sample and decreases from 64.4 to 31 ns for the Gd15 sample. Gd^{3+} doping provides prolonged average lifetime at a specific concentration. Also, the radiative component of the average lifetime and its contribution increase at the Gd10 sample, and these values decrease for the Gd15 sample. It can be originated

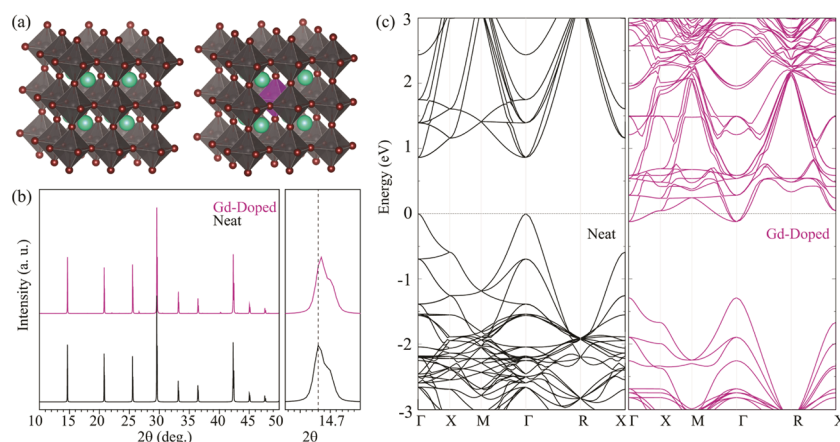


Figure 7. Crystal structures of neat (right) and Gd-doped (left) cubic CsPbI₃ (a). Computational X-ray diffractograms of neat and Gd-doped cubic CsPbI₃ (b). Electronic band dispersion of neat (E_F is set to zero) and Gd-doped cubic CsPbI₃ (c).

from reduced defects due to Gd³⁺ doping, but at the high doping levels, defects are generated again. Furthermore, Urbach energies of the samples are also consistent with the reduced defect amount most probably due to Gd³⁺ doping. In a similar manner, Lu et al.⁵³ reported that with Sr²⁺ doping the radiative component of lifetime and its contribution to the average lifetime increased in CsPbI₃ nanocrystals.

To investigate the effect of the Gd doping on structural and electronic properties of the CsPbI₃ crystal and verify the experimental results, density functional theory-based first-principles calculations are performed for neat and Gd³⁺-doped CsPbI₃ perovskite crystal structures presented in Figure 7a. DFT calculations reveal that the cohesive energies per atom are 3.22 and 3.32 eV for neat and Gd-doped CsPbI₃ structures, respectively. The 0.1 eV energy difference per atom reveals that, when the Gd atoms were included before the crystallization, the formation of Gd³⁺-doped CsPbI₃ nanocrystals is more favorable.

In addition, Bader charge analysis reveals that, for the neat crystal, each Pb atom donates 0.64 eV and Gd atom donates 1.40 eV to the Gd³⁺-doped CsPbI₃ crystal. Therefore, in the case of the Pb–Gd substitutional doping, 0.76 eV additional charge per Pb–Gd substitution on the crystal structure is observed. In this context, when we scrutinize the PbI₆ and GdI₆ octahedra, due to the extra charge around the Gd atom, Gd–I bond lengths are 7.52% decreased (3.19–2.95 Å) compared to the Pb–I bonds. This shrinkage is also confirmed by the slight right shift shown in both experimental and theoretical X-ray diffractograms (Figure 7b). Finally, electronic band structures presented in Figure 7c reveal that Gd–Pb substitutional doping is n-type doping that changes the electronic properties of the CsPbI₃ nanocrystal.

4. CONCLUSIONS

In summary, the main handicap in application of CsPbI₃ nanocrystals is inevitable phase transition from the metastable α -phase to the thermodynamically stable δ -phase. In this work, Gd³⁺ doping with various concentrations from 0 to 15 mol % is performed for stabilizing the α -phase. The Gd10 sample shows the highest phase stability among all samples. The substitution of Gd into the perovskite lattice is confirmed by peak shifting to the right side in the XRD pattern. Also, the same trend is observed in the computational XRD pattern of the Gd³⁺-doped CsPbI₃ crystal. This peak shifting is caused by lattice shrinkage

of Gd³⁺-doped crystals. Further, Gd³⁺ doping increases cohesive energy per atom from 3.22 to 3.32 eV, which indicates that the formation of Gd³⁺-doped nanocrystals is more favorable than neat CsPbI₃ nanocrystals. Prolonged stability of the α -phase may be originated from three factors. First is the distortion of cubic symmetry in the perovskite structure upon incorporation of the Gd³⁺ ion. This cubic phase distortion causes splitting of the reflection of the (200) plane. This hypothesis is compatible with results presented in the literature in the case of Bi³⁺ and Eu³⁺ doping.^{26,27} Second, Goldschmidt's tolerance factor is increased via Gd ($r_{\text{Gd}^{3+}} = 0.93$ Å) doping from 0.807 to 0.817, which can increase the stability of the perovskite structure in Gd³⁺-doped CsPbI₃ nanocrystals. Third, as a donor dopant, Gd³⁺ ions may associate with more I[−] ions than Pb²⁺ ions, and this can be the reason of reduced defect amount. Further, PLQY and average PL lifetime of Gd³⁺-doped nanocrystals increased due to low defect density. The doped samples have lower Urbach energies than the neat sample. These results suggest that the defect density of doped nanocrystals is reduced compared to that of neat nanocrystals; therefore, it is obvious that Gd³⁺ doping enhances optical properties and phase stability of α -CsPbI₃ nanocrystals. Finally, the electronic band structure of Gd-doped CsPbI₃ crystals shows n-type semiconductor behavior without any significant modifications in the band structure.

AUTHOR INFORMATION

Corresponding Authors

*E-mail: mdemir@iyte.edu.tr (M.M.D.).

*E-mail: hasansahin@iyte.edu.tr (H.S.).

ORCID

Mustafa M. Demir: 0000-0003-1309-3990

Author Contributions

§C.M.G. and Y.Y. contributed equally to the work.

Notes

The authors declare no competing financial interest.

ACKNOWLEDGMENTS

Computational resources were provided by TUBITAK ULAKBIM, High Performance and Grid Computing Center (TR-Grid e-Infrastructure). H.S. acknowledges financial support from the TUBITAK under Project No. 117F095. Characterization techniques (STEM and XRD) were per-

formed by the Izmir Institute of Technology, Center for Materials Research.

REFERENCES

- (1) Protesescu, L.; Yakunin, S.; Bodnarchuk, M. I.; Krieg, F.; Caputo, R.; Hendon, C. H.; Yang, R. X.; Walsh, A.; Kovalenko, M. V. Nanocrystals of Cesium Lead Halide Perovskites (CsPbX_3 , X = Cl, Br, and I): Novel Optoelectronic Materials Showing Bright Emission with Wide Color Gamut. *Nano Lett.* **2015**, *15*, 3692–3696.
- (2) Kovalenko, M. V.; Protesescu, L.; Bodnarchuk, M. I. Properties and Potential Optoelectronic Applications of Lead Halide Perovskite Nanocrystals. *Science* **2017**, *358*, 745–750.
- (3) Eperon, G. E.; Paternò, G. M.; Sutton, R. J.; Zampetti, A.; Haghighirad, A. A.; Caciali, F.; Snaith, H. J. Inorganic Cesium Lead Iodide Perovskite Solar Cells. *J. Mater. Chem. A* **2015**, *3*, 19688–19695.
- (4) Saidaminov, M. I.; Haque, M. A.; Savoie, M.; Abdelhady, A. L.; Cho, N.; Dursun, I.; Buttner, U.; Alarousu, E.; Wu, T.; Bakr, O. M. Perovskite Photodetectors Operating in Both Narrowband and Broadband Regimes. *Adv. Mater.* **2016**, *28*, 8144–8149.
- (5) Song, J.; Li, J.; Li, X.; Xu, L.; Dong, Y.; Zeng, H. Quantum Dot Light-Emitting Diodes Based on Inorganic Perovskite Cesium Lead Halides (CsPbX_3). *Adv. Mater.* **2015**, *27*, 7162–7167.
- (6) Li, X.; Cao, F.; Yu, D.; Chen, J.; Sun, Z.; Shen, Y.; Zhu, Y.; Wang, L.; Wei, Y.; Wu, Y.; et al. All Inorganic Halide Perovskites Nanosystem: Synthesis, Structural Features, Optical Properties and Optoelectronic Applications. *Small* **2017**, *13*, No. 1603996.
- (7) Dutta, A.; Pradhan, N. Phase-Stable Red-Emitting CsPbI_3 Nanocrystals: Successes and Challenges. *ACS Energy Lett.* **2019**, *4*, 709–719.
- (8) Swarnkar, A.; Mir, W. J.; Nag, A. Can B-Site Doping or Alloying Improve Thermal- and Phase-Stability of All-Inorganic CsPbX_3 (X = Cl, Br, I) Perovskites? *ACS Energy Lett.* **2018**, *3*, 286–289.
- (9) Pan, G.; Bai, X.; Yang, D.; Chen, X.; Jing, P.; Qu, S.; Zhang, L.; Zhou, D.; Zhu, J.; Xu, W.; et al. Doping Lanthanide into Perovskite Nanocrystals: Highly Improved and Expanded Optical Properties. *Nano Lett.* **2017**, *17*, 8005–8011.
- (10) Imran, M.; Caligiuri, V.; Wang, M.; Goldoni, L.; Prato, M.; Krahne, R.; De Trizio, L.; Manna, L. Benzoyl Halides as Alternative Precursors for the Colloidal Synthesis of Lead-Based Halide Perovskite Nanocrystals. *J. Am. Chem. Soc.* **2018**, *140*, 2656–2664.
- (11) Pan, J.; Shang, Y.; Yin, J.; De Bastiani, M.; Peng, W.; Dursun, I.; Sinatra, L.; El-Zohry, A. M.; Hedhili, M. N.; Emwas, A.-H.; et al. Bidentate Ligand-Passivated CsPbI_3 Perovskite Nanocrystals for Stable Near-Unity Photoluminescence Quantum Yield and Efficient Red Light-Emitting Diodes. *J. Am. Chem. Soc.* **2018**, *140*, 562–565.
- (12) Yin, J.; Ahmed, G. H.; Bakr, O. M.; Brédas, J. L.; Mohammed, O. F. Unlocking the Effect of Trivalent Metal Doping in All-Inorganic CsPbBr_3 Perovskite. *ACS Energy Lett.* **2019**, *4*, 789–795.
- (13) Duan, J.; Zhao, Y.; Yang, X.; Wang, Y.; He, B.; Tang, Q. Lanthanide Ions Doped CsPbBr_3 Halides for HTM-Free 10.14%-Efficiency Inorganic Perovskite Solar Cell with an Ultrahigh Open-Circuit Voltage of 1.594 V. *Adv. Energy Mater.* **2018**, *8*, No. 1802346.
- (14) Hu, Q.; Li, Z.; Tan, Z.; Song, H.; Ge, C.; Niu, G.; Han, J.; Tang, J. Rare Earth Ion-Doped CsPbBr_3 Nanocrystals. *Adv. Opt. Mater.* **2018**, *6*, No. 1700864.
- (15) Pradhan, N.; Das Adhikari, S.; Nag, A.; Sarma, D. D. Luminescence, Plasmonic, and Magnetic Properties of Doped Semiconductor Nanocrystals. *Angew. Chem., Int. Ed.* **2017**, *56*, 7038–7054.
- (16) Akkerman, Q. A.; Meggiolaro, D.; Dang, Z.; De Angelis, F.; Manna, L. Fluorescent Alloy $\text{CsPb}_{1-x}\text{Mn}_x$ Perovskite Nanocrystals with High Structural and Optical Stability. *ACS Energy Lett.* **2017**, *2*, 2183–2186.
- (17) Bai, D.; Zhang, J.; Jin, Z.; Bian, H.; Wang, K.; Wang, H.; Liang, L.; Wang, Q.; Liu, S. F. Interstitial Mn^{2+} -Driven High-Aspect-Ratio Grain Growth for Low-Trap-Density Microcrystalline Films for Record Efficiency CsPbI_2Br Solar Cells. *ACS Energy Lett.* **2018**, *3*, 970–978.
- (18) Guner, T.; Akbali, B.; Ozcan, M.; Topcu, G.; Demir, M. M.; Sahin, H. Monitoring the Doping and Diffusion Characteristics of Mn Dopants in Cesium Lead Halide Perovskites. *J. Phys. Chem. C* **2018**, *122*, 11543–11549.
- (19) Liu, F.; Ding, C.; Zhang, Y.; Ripolles, T. S.; Kamisaka, T.; Toyoda, T.; Hayase, S.; Minemoto, T.; Yoshino, K.; Dai, S.; et al. Colloidal Synthesis of Air-Stable Alloyed $\text{CsSn}_{1-x}\text{Pb}_x\text{I}_3$ Perovskite Nanocrystals for Use in Solar Cells. *J. Am. Chem. Soc.* **2017**, *139*, 16708–16719.
- (20) Shen, X.; Zhang, Y.; Kershaw, S. V.; Li, T.; Wang, C.; Zhang, X.; Wang, W.; Li, D.; Wang, Y.; Lu, M.; et al. Zn-Alloyed CsPbI_3 Nanocrystals for Highly Efficient Perovskite Light-Emitting Devices. *Nano Lett.* **2019**, *19*, 1552–1559.
- (21) Liu, F.; Ding, C.; Zhang, Y.; Kamisaka, T.; Zhao, Q.; Luther, J. M.; Toyoda, T.; Hayase, S.; Minemoto, T.; Yoshino, K.; et al. GeI_2 Additive for High Optoelectronic Quality CsPbI_3 Quantum Dots and Their Application in Photovoltaic Devices. *Chem. Mater.* **2019**, *31*, 798–807.
- (22) Lau, C. F. J.; Zhang, M.; Deng, X.; Zheng, J.; Bing, J.; Ma, Q.; Kim, J.; Hu, L.; Green, M. A.; Huang, S.; et al. Strontium-Doped Low-Temperature-Processed CsPbI_2Br Perovskite Solar Cells. *ACS Energy Lett.* **2017**, *2*, 2319–2325.
- (23) Jiang, Q.; Zeng, X.; Wang, N.; Xiao, Z.; Guo, Z.; Lu, J. Electrochemical Lithium Doping Induced Property Changes in Halide Perovskite CsPbBr_3 Crystal. *ACS Energy Lett.* **2018**, *3*, 264–269.
- (24) Li, Y.; Duan, J.; Yuan, H.; Zhao, Y.; He, B.; Tang, Q. Lattice Modulation of Alkali Metal Cations Doped $\text{CsI}-x\text{RbPbBr}_3$ Halides for Inorganic Perovskite Solar Cells. *Solar RRL* **2018**, *2*, No. 1800164.
- (25) Abdi-Jalebi, M.; Andaji-Garmaroudi, Z.; Cacovich, S.; Stavrakas, C.; Philippe, B.; Richter, J. M.; Mejd, A.; Booker, E. P.; Hutter, E. M.; Pearson, A. J.; et al. Maximizing and Stabilizing Luminescence from Halide Perovskites with Potassium Passivation. *Nature* **2018**, *555*, 497.
- (26) Jiang, Q.; Chen, M.; Li, J.; Wang, M.; Zeng, X.; Besara, T.; Lu, J.; Xin, Y.; Shan, X.; Pan, B.; et al. Electrochemical Doping of Halide Perovskites with Ion Intercalation. *ACS Nano* **2017**, *11*, 1073–1079.
- (27) Yang, Y.; Zou, X.; Pei, Y.; Bai, X.; Jin, W.; Chen, D. Effect of Doping of NaI Monovalent Cation Halide on the Structural, Morphological, Optical and Optoelectronic Properties of MAPbI_3 Perovskite. *J. Mater. Sci.: Mater. Electron.* **2018**, *29*, 205–210.
- (28) Amgar, D.; Binyamin, T.; Uvarov, V.; Etgar, L. Near Ultra-Violet to Mid-Visible Band Gap Tuning of Mixed Cation $\text{RbxCs}_{1-x}\text{PbX}_3$ (X = Cl or Br) Perovskite Nanoparticles. *Nanoscale* **2018**, *10*, 6060–6068.
- (29) Liu, M.; Zhong, G.; Yin, Y.; Miao, J.; Li, K.; Wang, C.; Xu, X.; Shen, C.; Meng, H. Aluminum-Doped Cesium Lead Bromide Perovskite Nanocrystals with Stable Blue Photoluminescence Used for Display Backlight. *Adv. Sci.* **2017**, *4*, No. 1700335.
- (30) Yao, J. S.; Ge, J.; Han, B.-N.; Wang, K. H.; Yao, H. B.; Yu, H. L.; Li, J. H.; Zhu, B. S.; Song, J. Z.; Chen, C.; et al. Ce^{3+} -Doping to Modulate Photoluminescence Kinetics for Efficient CsPbBr_3 Nanocrystals Based Light-Emitting Diodes. *J. Am. Chem. Soc.* **2018**, *140*, 3626–3634.
- (31) Xiang, W.; Wang, Z.; Kubicki, D. J.; Tress, W.; Luo, J.; Prochowicz, D.; Akin, S.; Emsley, L.; Zhou, J.; Dietler, G.; et al. Europium-Doped CsPbI_2Br for Stable and Highly Efficient Inorganic Perovskite Solar Cells. *Joule* **2019**, *3*, 205–214.
- (32) Hu, Y.; Bai, F.; Liu, X.; Ji, Q.; Miao, X.; Qiu, T.; Zhang, S. Bismuth Incorporation Stabilized α - CsPbI_3 for Fully Inorganic Perovskite Solar Cells. *ACS Energy Lett.* **2017**, *2*, 2219–2227.
- (33) Lozhkina, O. A.; Murashkina, A. A.; Shilovskikh, V. V.; Kapitonov, Y. V.; Ryabchuk, V. K.; Emeline, A. V.; Miyasaka, T. Invalidity of Band-Gap Engineering Concept for Bi^{3+} Heterovalent Doping in CsPbBr_3 Halide Perovskite. *J. Phys. Chem. Lett.* **2018**, *9*, 5408–5411.
- (34) Jena, A. K.; Kulkarni, A.; Sanehira, Y.; Ikegami, M.; Miyasaka, T. Stabilization of α - CsPbI_3 in Ambient Room Temperature Conditions by Incorporating Eu into CsPbI_3 . *Chem. Mater.* **2018**, *30*, 6668–6674.

- (35) Zhang, X.; Zhang, Y.; Zhang, X.; Yin, W.; Wang, Y.; Wang, H.; Lu, M.; Li, Z.; Gu, Z.; Yu, W. W. Yb³⁺ and Yb³⁺/Er³⁺ Doping for Near-Infrared Emission and Improved Stability of CsPbCl₃ Nanocrystals. *J. Mater. Chem. C* **2018**, *6*, 10101–10105.
- (36) Zhang, X.; Wang, H.; Hu, Y.; Pei, Y.; Wang, S.; Shi, Z.; Colvin, V. L.; Wang, S.; Zhang, Y.; Yu, W. W. Strong Blue Emission from Sb³⁺-Doped Super Small CsPbBr₃ Nanocrystals. *J. Phys. Chem. Lett.* **2019**, *10*, 1750–1756.
- (37) Ozen, S.; Guner, T.; Topcu, G.; Ozcan, M.; Demir, M.; Sahin, H. Experimental and First-Principles Investigation of Cr-Driven Color Change in Cesium Lead Halide Perovskites. *J. Appl. Phys.* **2019**, *125*, No. 225705.
- (38) Kresse, G.; Joubert, D. From Ultrasoft Pseudopotentials to the Projector Augmented-Wave Method. *Phys. Rev. B* **1999**, *59*, 1758.
- (39) Blöchl, P. E. Projector Augmented-Wave Method. *Phys. Rev. B* **1994**, *50*, 17953.
- (40) Kresse, G.; Hafner, J. Ab Initio Molecular Dynamics for Liquid Metals. *Phys. Rev. B* **1993**, *47*, 558.
- (41) Kresse, G.; Furthmüller, J. Efficient Iterative Schemes for Ab Initio Total-Energy Calculations using a Plane-Wave Basis Set. *Phys. Rev. B* **1996**, *54*, 11169.
- (42) Perdew, J. P.; Burke, K.; Ernzerhof, M. Generalized Gradient Approximation Made Simple. *Phys. Rev. Lett.* **1996**, *77*, 3865.
- (43) Henkelman, G.; Arnaldsson, A.; Jónsson, H. A Fast and Robust Algorithm for Bader Decomposition of Charge Density. *Comput. Mater. Sci.* **2006**, *36*, 354–360.
- (44) Goldschmidt, V. M. Die gesetze der krystallochemie. *Naturwissenschaften* **1926**, *14*, 477–485.
- (45) Guner, T.; Demir, M. M. A Review on Halide Perovskites as Color Conversion Layers in White Light Emitting Diode Applications. *Phys. Status Solidi A* **2018**, *215*, No. 1800120.
- (46) Li, Z.; Yang, M.; Park, J.-S.; Wei, S.-H.; Berry, J. J.; Zhu, K. Stabilizing Perovskite Structures by Tuning Tolerance Factor: Formation of Formamidinium and Cesium Lead Iodide Solid-State Alloys. *Chem. Mater.* **2016**, *28*, 284–292.
- (47) Imran, M.; Di Stasio, F.; Dang, Z.; Canale, C.; Khan, A. H.; Shamsi, J.; Brescia, R.; Prato, M.; Manna, L. Colloidal Synthesis of Strongly Fluorescent CsPbBr₃ Nanowires with Width Tunable Down to the Quantum Confinement Regime. *Chem. Mater.* **2016**, *28*, 6450–6454.
- (48) Weidman, M. C.; Seitz, M.; Stranks, S. D.; Tisdale, W. A. Highly Tunable Colloidal Perovskite Nanoplatelets through Variable Cation, Metal, and Halide Composition. *ACS Nano* **2016**, *10*, 7830–7839.
- (49) Yang, C.; Faust, A.; Amit, Y.; Gdor, I.; Banin, U.; Ruhman, S. Impurity Sub-Band in Heavily Cu-Doped InAs Nanocrystal Quantum Dots Detected by Ultrafast Transient Absorption. *J. Phys. Chem. A* **2016**, *120*, 3088–3097.
- (50) Begum, R.; Parida, M. R.; Abdelhady, A. L.; Murali, B.; Alyami, N. M.; Ahmed, G. H.; Hedhili, M. N.; Bakr, O. M.; Mohammed, O. F. Engineering Interfacial Charge Transfer in CsPbBr₃ Perovskite Nanocrystals by Heterovalent Doping. *J. Am. Chem. Soc.* **2017**, *139*, 731–737.
- (51) Kamat, P. V.; Dimitrijevic, N. M.; Nozik, A. Dynamic Burstein-Moss Shift in Semiconductor Colloids. *J. Phys. Chem. A* **1989**, *93*, 2873–2875.
- (52) Urbach, F. The Long-Wavelength Edge of Photographic Sensitivity and of the Electronic Absorption of Solids. *Phys. Rev.* **1953**, *92*, 1324.
- (53) Lu, M.; Zhang, X.; Zhang, Y.; Guo, J.; Shen, X.; Yu, W. W.; Rogach, A. L. Simultaneous Strontium Doping and Chlorine Surface Passivation Improve Luminescence Intensity and Stability of CsPbI₃ Nanocrystals Enabling Efficient Light-Emitting Devices. *Adv. Mater.* **2018**, *30*, No. 1804691.